IEEE Robotics and Automation Letters (RA-L) paper, presented at ICRA 2026, Vienna, Austria. Cite as RA-L paper.

STEM: A Soft Tactile Electromagnetic Actuator for Multimodal Haptic Feedback in Virtual Environments

Heeju Mun, *Graduate Student Member, IEEE*, Seung Mo Jeong, Sein Lim, *Graduate Student Member, IEEE*, Seunggyeom Jung, *Graduate Student Member, IEEE*, and Ki-Uk Kyung, *Member, IEEE*

***Abstract*—This study introduces the soft tactile electromagnetic (STEM) actuator, a compact and wearable haptic device designed to deliver multimodal tactile feedback in virtual environments. The actuator employs soft materials as both an energy-storing and encasing structure, enabling out-of-plane deformations in response to arbitrary input signals while ensuring high wearability. Magnetic reinforcements, including a soft magnetic cap and a ferromagnetic pole piece, minimize magnetic flux leakage, effectively amplifying output force along with protrusion to enable precise and varied haptic feedback. The actuator generates multimodal tactile stimuli, including force, impulse, and vibration, surpassing conventional vibrotactile devices in delivering more varied and dynamic feedback. Experimental evaluation of the actuator's mechanical performance demonstrates its ability to produce both low- and high-frequency tactile feedback. A user study evaluating perception thresholds and signal recognition accuracy found that participants identified eight distinct tactile signals with an average accuracy of 91%, confirming the actuator's capacity to deliver distinguishable multimodal feedback. These findings underscore the feasibility of the STEM actuator for immersive haptic interactions and highlight its potential applications in virtual reality.**

***Index Terms*—Multimodal tactile, soft actuator, wearable.**

I. Introduction

With the continuous advancement of virtual reality (VR), research into wearable haptic devices that simulate tactile interactions for immersive virtual experiences remains ongoing [1], [2]. Humans primarily interact with the physical world through haptic feedback, underscoring the significance of wearable haptic devices in enhancing immersion and interaction in VR technologies [3]. By providing only tactile or cutaneous feedback, these devices enable users to manipulate three-dimensional virtual objects more intuitively, reducing cognitive load and reliance on vision for certain tasks [4], [5], [6], [7].

Wearability is critical factor influencing immersion in VR environments. Rigid and bulky devices with low wearability not only pose safety risks but also disrupt the cognitive connection between virtual and physical interactions due to high impedance [8]. To address issue, compact vibrotactile actuators, such as linear resonant actuators (LRAs) and coin motors, are commonly employed [9], [10], [11], [12], [13]. These actuators generate strong vibrations at specific frequencies, sufficient for notifying users of interactions. For less dynamic feedback, small-scale motors are utilized, while spatial haptic surfaces—such as virtual bumps and patterned textures—are rendered using linear motors that generate indentational forces at the fingertips to deform the skin [14]. Another method for delivering a pressing sensation involves using a servo motor enclosed in a thimble-like structure [15], [16]. Although these approaches provide single-mode tactile feedback, recent research has focused on developing devices with greater degrees of freedom. A common strategy is integrating multiple actuators or motors to generate different tactile stimuli, such as pressure, vibration, and shear [17], [18], [19], [20]. However, this approach increases system size, reducing accessibility and wearability.

To overcome these limitations, soft materials have been increasingly utilized in wearable haptic actuators offering promising solutions for compliant and lightweight designs. Soft tactile actuators enable conformal contact with finger curvature, which is crucial for effective feedback transmission. Various strategies have been explored for developing such actuators. Dielectric and electrostatic actuators provide fast responses and high energy density at high voltage inputs (∼kV) [21], [22], [23], [24], [25]. Pneumatic actuators generate substantial force output (∼N) but are limited by a narrow bandwidth in the tens of Hertz range, and their bulky air compressors restrict mobility [26], [27], [28]. While soft functional materials present an innovative actuation approach, challenges such as low force output, durability, and feasibility remain [8].

Rather than using soft materials as the primary actuating element, they can serve as passive structures for encapsulation or energy storage. Yu et al. and Li et al. introduced miniaturized electromagnetic tactile actuators that incorporate flexible films as elastic structures [29], [30] However, these designs prioritize miniaturization and minimal power consumption, limiting them to vibration at a specific resonance frequency.

Received 22 February 2025; accepted 19 June 2025. Date of publication 23 July 2025; date of current version 20 August 2025. This article was recommended for publication by Associate Editor S. Funabashi and Editor T. Ogata upon evaluation of the reviewers' comments. This work was supported by the Institute of Information & communications Technology Planning & Evaluation (IITP) grant funded by the Korea Government(MSIT) under Grant RS-2025-02303658. *(Corresponding author: Ki-Uk Kyung.)*

This work involved human subjects or animals in its research. Approval of all ethical and experimental procedures and protocols was granted by the KAIST Institutional Review Board (IRB) under Application No. KH2023-177, and performed in line with the Declaration of Helsinki.

The authors are with the Department of Mechanical Engineering, Korea Advanced Institute of Science and Technology, Daejeon 34141, South Korea (e-mail: heeju.1234@kaist.ac.kr; seungmoj@kaist.ac.kr; onsein@kaist.ac.kr; jsgyeom@kaist.ac.kr; kyungku@kaist.ac.kr).

This article has supplementary downloadable material available at https://doi.org/10.1109/LRA.2025.3592103, provided by the authors.

Digital Object Identifier 10.1109/LRA.2025.3592103

IEEE Robotics and Automation Letters (RA-L) paper, presented at ICRA 2026, Vienna, Austria. Cite as RA-L paper.

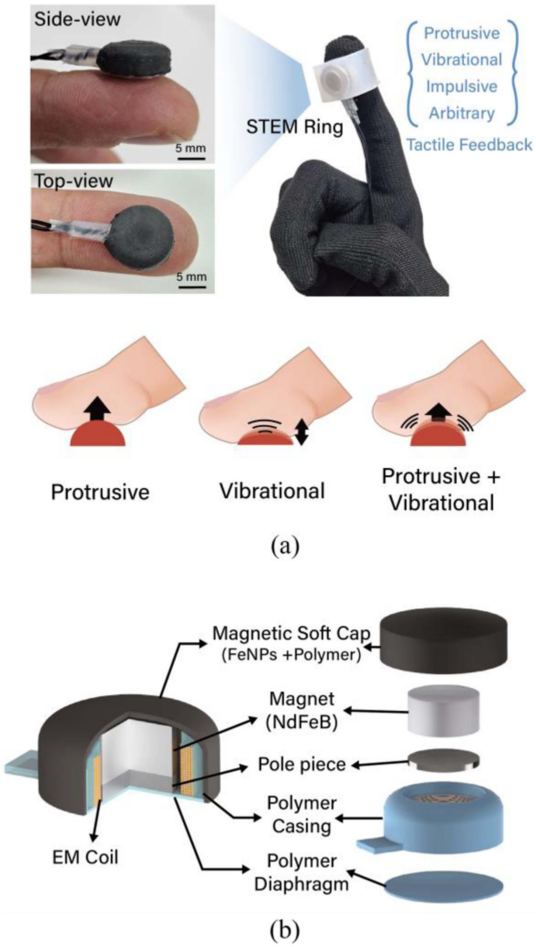

Fig. 1. (a) Photograph of the soft tactile electromagnetic (STEM) actuator, designed to provide multimodal tactile feedback with enhanced wearability. When worn as a STEM ring on the finger, it can deliver protrusive force, vibrational feedback, or a combination of both simultaneously. (b) Structural diagram of the STEM actuator.

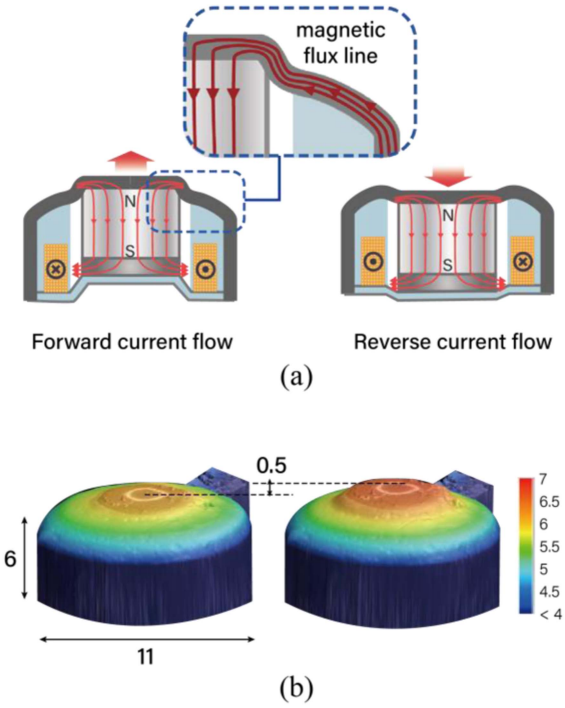

Fig. 2. (a) Schematic illustrating the working mechanism of the actuator and the role of magnetic reinforcement in enhancing output force by directing magnetic flux lines along the soft magnetic cap and pole piece. (b) 3D shape of the actuator to visualize the protrusion (dimensions are in mm scale).

In this study, we propose a soft tactile electromagnetic (STEM) actuator that is finger-worn and capable of delivering not only vibrational feedback but also force, impulse, and arbitrary tactile sensations (see Fig. 1(a)). By integrating soft materials as both an energy-storing component and an encasing structure, the actuator achieves out-of-plane deformations, enhancing wearability while enabling a range of tactile stimuli, including protrusive force. The developed hardware aims to provide diverse haptic sensations that are challenging to achieve with single-mode feedback, such as rendering micro-textures composed of high-frequency vibrations, macro-textures featuring small bumps, or a combination of both simultaneously.

This letter is structured as follows: Section II examines the actuator design, while Sections III and IV discuss its mechanical and psychophysical performance. Finally, Section V concludes with an overview of the STEM actuator's limitations and potential future developments.

II. Haptic Actuator Design

A. Design Overview

The proposed actuator comprises an electromagnetic copper coil embedded in a polymer casing, a permanent magnet with a pole piece, and a magnetic soft cap covering most of the system, as illustrated in Fig. 1(b). The magnet is suspended within the electromagnetic (EM) coil by a polymer diaphragm, enabling controlled motion. When the coil is activated, the magnet undergoes longitudinal displacement due to the Lorentz force (see Fig. 2(a)).

The actuator's elastomer-based structure allows the magnet to protrude, enabling diverse haptic feedback, including impulsive forces (such as tapping) and protrusive forces (such as pressure). Additionally, the elastic diaphragm enhances dynamic performance by leveraging resonance to generate strong vibrational feedback.

A key design feature of the STEM actuator is its magnetic reinforcements, which include a magnetic soft cap—a polymer composite infused with iron nanoparticles (FeNPs)—and a pole piece. These components guide the magnetic flux lines perpendicular to the current-carrying wires of the EM coil, minimizing flux leakage. By directing the flux lines along the magnetic soft body and forming a nearly closed magnetic loop (see Fig. 2(a)), the actuator achieves higher force output and improved efficiency. The protrusion of the actuator is clearly visualized from its 3D shape (see Fig. 2(b)), obtained using a 3D optical profilometer (VR-6000, Keyence). It can produce a protrusion of approximately 0.5 mm under a constant current input of 750 mA.

B. Magnetic Reinforcements

To enhance the actuator's output force, magnetic reinforcements, including a pole piece and a magnetic soft cap, are incorporated. The pole piece, made of soft iron with high relative permeability ($1–10 \times 10^3$), directs the magnetic flux lines from

IEEE Robotics and Automation Letters (RA-L) paper, presented at ICRA 2026, Vienna, Austria. Cite as RA-L paper.

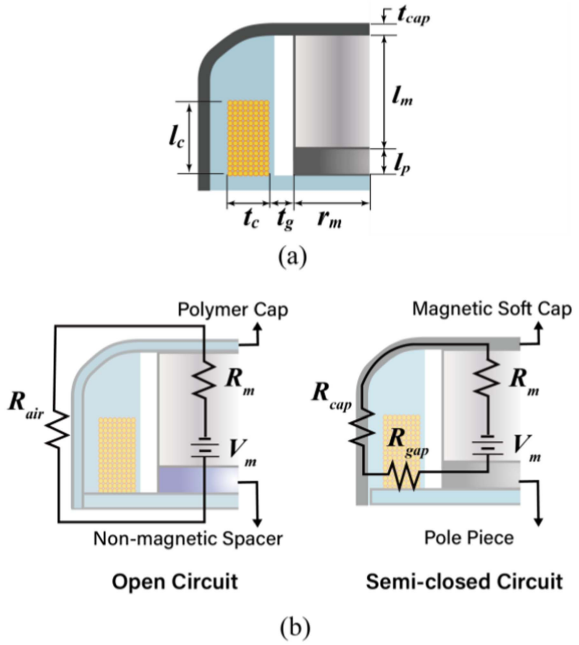

Fig. 3. (a) Simplified cross-sectional geometry of STEM actuator and (b) simplified magnetic circuit representation of the actuator without (open circuit) and with magnetic reinforcements (semi-closed circuit).

the permanent magnet (Neodymium magnet, NdFeB, N42). This configuration ensures that most flux lines are aligned perpendicularly to the current $\bar{I}$ flowing through the coil of length l, under the magnetic flux density $\bar{B}$. This alignment maximizes the Lorentz force F_{mag}, given by (1):

$$F_{mag} = \bar{I} \cdot \int dl \times \bar{B} \tag{1}$$

The magnetic soft cap, composed of an FeNP–polymer composite (EcoFlex 00-50, SmoothOn Inc.), minimizes magnetic flux leakage. Acting as a flux shield, it provides a low-resistance path for magnetic fields, thereby enhancing the actuator's force output. By introducing magnetic properties to the cap, which covers most of the actuator's upper portion, flux lines are effectively contained within the system. The impact of these magnetic reinforcements is theoretically analyzed and validated through simulations.

The actuator's geometry and its lumped parameter model are shown in Fig. 3(a), with key dimensions: l_p (pole piece length), l_m (magnet axial length), r_m (magnet radius), t_{cap} (soft cap thickness), t_c (coil width), and t_g (air gap). To simplify calculations, the following assumptions are made:

- Flux leakage and fringing effects are neglected.
- The pole piece's relative permeability is significantly higher than that of the vacuum ($\mu_{iron} \gg \mu_0$)
- The air and polymer body's permeability are approximated as equal to the vacuum permeability ($\mu_{air} = \mu_{polymer} = \mu_0$)
- Inductance effects in the coil are ignored.

By comparing the equivalent magnetic circuits of designs with and without magnetic reinforcements (Fig. 3(b)), their effects on

TABLE I
RELUCTANCE AND MAGNETIC SOURCE VALUES

Parameter	Value	Parameter	Value
V_m	$\frac{B_r l_m}{\mu_m}$	R_{gap}	$\frac{ln\left(1+\frac{t_g+t_c}{r_m}\right)}{2\pi\mu_0 l_p}$
R_m	$\frac{l_m}{\pi\mu_m r_m^2}$	R_{cap}	$\frac{l_p+l_m}{2\pi\mu_{cap}t_{cap}(r_m+t_c+t_g)}+\frac{ln\left(1+\frac{t_g+t_c}{r_m}\right)}{2\pi\mu_{cap}t_{cap}}$
R_{air}	$\gg R_{cap}+R_{gap}$		

performance can be predicted. The open circuit design allows field lines to disperse into the air, while the semi-closed circuit guides them through the magnetic soft cap. The permanent magnet is modeled as a non-ideal magnetic voltage source $V_m$with an internal reluctance R_m. The open circuit has an air reluctance R_{air}, whereas the semi-closed circuit has a reluctance R_{gap} (air gap) and R_{cap} (magnetic soft cap). These lumped parameters are provided in Table I, where $B_r$is the remanent flux density of the permanent magnet, $\mu_m = 1.4\,\mu_0$ is the permeability of the magnet, and $\mu_{cap}(> \mu_0)$ represents the permeability of the magnetic soft cap, which depends on the FeNP volume concentration in the polymer composite.

The total magnetic flux ϕ is given by (2):

$$\phi = \frac{V_m}{R_{net}}, \tag{2}$$

where R_{net} is the net reluctance, which is $R_{air} + R_m$ for the open circuit and $R_{cap} + R_{gap} + R_m$ for the semi-closed circuit. For the open and semi-closed circuits, the flux values can be computed using (3).

$$\phi_{closed} = \frac{V_m}{R_{cap}+R_{gap}+R_m} \gg \frac{V_m}{R_{air}+R_m} = \phi_{open}. \tag{3}$$

This confirms that the semi-closed design achieves significantly higher flux. The magnetic flux density in the coil region B_g for the semi-closed design is obtained using (4) from which we can derive the output force using (1):

$$B_g = \frac{\phi_{closed}}{2\pi\left(r_m + t_g + \frac{t_c}{2}\right) l_p} \tag{4}$$

To verify these theoretical predictions, finite element analysis (FEA) was conducted using COMSOL Multiphysics. The relative permeabilities of the soft cap and pole piece were set to 3 and 5000, respectively. Fig. 4(a) illustrates the simulation results, where the magnetic flux density norm is represented by the color scale and flux lines are drawn. The results indicate that flux lines are directed toward the soft magnetic cap, minimizing flux leakage. A comparison of the maximum magnetic flux densities in the semi-closed and open circuit designs, which was 2.18 T and 1.38 T respectively, demonstrates the effectiveness of the reinforcements in reducing leakage. Additionally, the arrow plot of radial magnetic flux density confirms that the reinforcements significantly enhance the flux available for Lorentz force generation.

To theoretically verify the effect of magnetic reinforcements, the output force performance of the actuator—with a

IEEE Robotics and Automation Letters (RA-L) paper, presented at ICRA 2026, Vienna, Austria. Cite as RA-L paper.

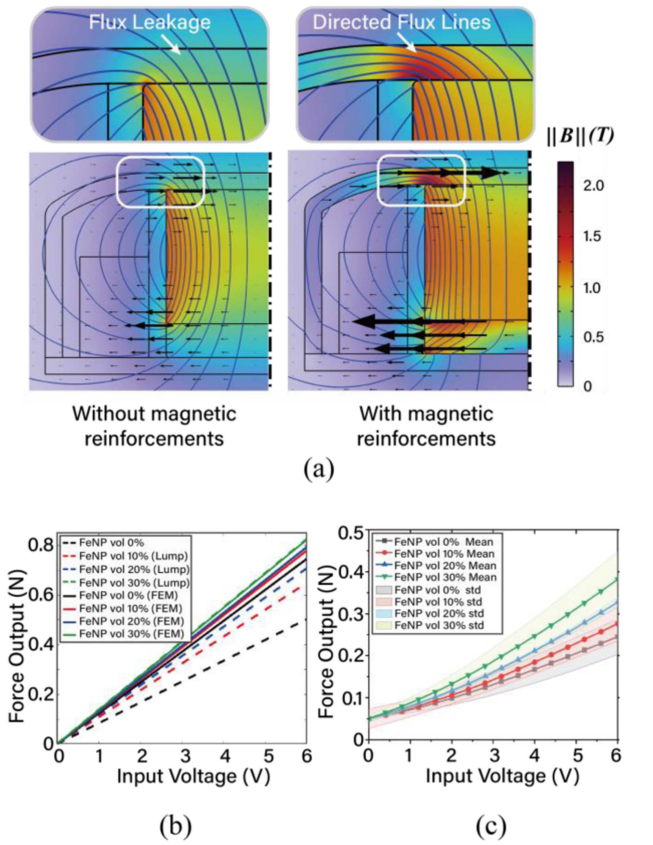

Fig. 4. (a) Simulation results illustrating the magnetic flux density norm as a surface plot, magnetic flux lines as contour lines, and radial magnetic flux density as an arrow plot for the actuator with and without magnetic reinforcements. (b) Output force predicted based on the lumped parameter model and FEM simulation. (c) Experimental results showing the effect of FeNP volume concentration on enhancing force output, where four measurements are taken at each input voltage for three samples with each volume concentration. The solid line represents the average static force and the shaded region represents the standard deviation.

soft magnetic cap containing increasing volume concentrations of FeNPs—was predicted using a lumped parameter model and compared with FEM simulation results, as illustrated in Fig. 4(b). As the theoretical model relies on several simplifying assumptions, its predictions deviate notably from the FEM results. Nevertheless, the findings support the hypothesis that enhanced performance can be achieved by incorporating magnetic reinforcements, as output force increases with higher FeNP concentrations.

To experimentally validate these findings, the actuator's static output force was measured for samples with varying FeNP concentrations (0–30 vol% in 10% increments) embedded in the polymer matrix. Higher FeNP content improves the soft cap's magnetic flux shielding capability, thereby reducing flux leakage and enhancing output force. The relative permeability values corresponding to different FeNP concentrations were measured using a Magnetic Property Measurement System (MPMS3-Evercool, Quantum Design Inc.), and the results are presented in Table II.

The output force was measured using a load cell (UMI-200gf, Dacell) attached to a vertical manual stage (Fig. 5(a)). An

TABLE II
RELATIVE PERMEABILITY OF MAGNETIC POLYMER COMPOSITE

FeNP vol %	Value
0	~1
10	1.52
20	1.79
30	2.47

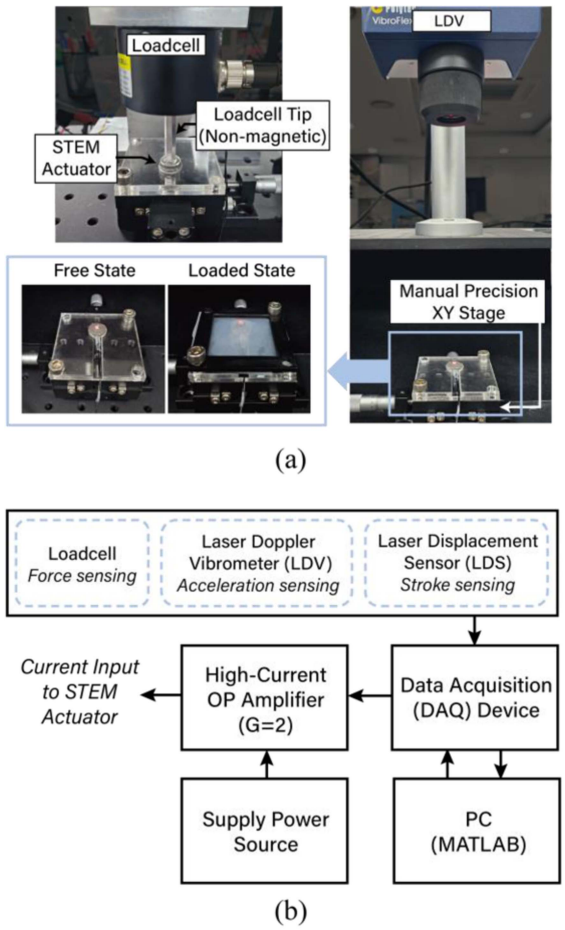

Fig. 5. (a) Experimental setup for measuring output force, acceleration, and protrusion. (b) Schematic of system setup.

initial 50 mN load was applied to simulate actuator-skin contact conditions. Instead of controlling the input current, voltage was varied for simplicity. A step input voltage was applied in 0.4 V increments, and the static force output was recorded for 30 s. Each measurement was repeated four times for three samples at each FeNP concentration.

The averaged static force output for different FeNP concentrations at increasing voltages is plotted in Fig. 4(c), where the solid line represents the mean, and the shaded region indicates the standard deviation. The results confirm that increasing the FeNP concentration in the soft cap enhances the actuator's force output. This supports the effectiveness of using magnetic reinforcements—such as the magnetic soft cap and pole piece—in minimizing flux leakage and improving actuator performance.

III. Haptic Actuator Output Performance

A. Experimental Set-up

To evaluate the output performance of the fabricated actuator, we set up the following measurement devices: a loadcell (UMI-200gf, Dacell) to measure force output, a laser Doppler vibrometer (LDV, Polytech) to measure acceleration output, and a laser displacement sensor (LDS, Keyence) to measure protrusion output. Below the equipment, the STEM actuator is firmly fixed to a manual precision XY using a jig, as illustrated in Fig. 5(a). This manual stage allows precise alignment of the actuator with the laser focus of the LDS and LDV, or co-axial alignment with the load cell tip.

As previously mentioned, a preload of 50 mN was applied before measuring the actuator's output performance. For force output measurements, this preload was directly applied by monitoring the force measured by the load cell. However, for non-contact measurements—such as protrusion or acceleration evaluation—a different approach was required to apply the preload without interfering with optical measurements while ensuring stability under dynamic motion. To achieve this, an elastomer membrane was placed over the actuator, with its edges firmly secured to the jig, simulating the loaded state (Fig. 5(a)). In contrast, the free state refers to the condition where no preload is applied to the actuator.

A data acquisition (DAQ) system (USB-6212, National Instruments) was used to collect measurement data and generate sinusoidal analog signals, which were fed into an operational amplifier (OPA547, Texas Instruments Inc.). The amplifier applied a gain of two to the signal before delivering the current input to the actuator. The entire system was controlled using MATLAB, as shown in Fig. 5(b). By varying the amplitude and frequency of the sinusoidal input, the dynamic output performance of the actuator was assessed.

B. Dynamic Response

The actuator's response to sinusoidal current inputs with amplitudes of 350 mA, 600 mA, and 750 mA was measured across varying frequencies.

For force output, the actuator produced a maximum force of 0.4 N at 0.1 Hz with a 750 mA input current, significantly exceeding the perceivable normal force at the fingertip—approximately 0.01 N under static conditions and 0.005 N under vibrational conditions [31]. The actuator demonstrated a bandwidth of 25 Hz, as shown in Fig. 6(a).

For protrusion output, the actuator exhibited a maximum displacement of 0.4 mm at 0.1 Hz under nearly static sinusoidal actuation, with a peak displacement of 0.63 mm at resonance in the free state (Fig. 6(b)). When a preload was applied, a slight reduction in performance was observed, as expected. Additionally, the resonance frequency shifted from 240 Hz at 350 mA to 190 Hz at 750 mA, likely due to nonlinearities in the actuator's mechanical system.

For acceleration output, sinusoidal input signals were applied up to 500 Hz, with results of RMS value shown in Fig. 6(c). The actuator consistently exceeded 10 m/s^2 above 30 Hz, reaching a peak acceleration of ∼1250 m/s^2 at resonance with a 750 mA input current under free state. This outstanding acceleration performance is attributed to the actuator's design, which incorporates a mass-spring system composed of a magnet and a soft magnetic cap.

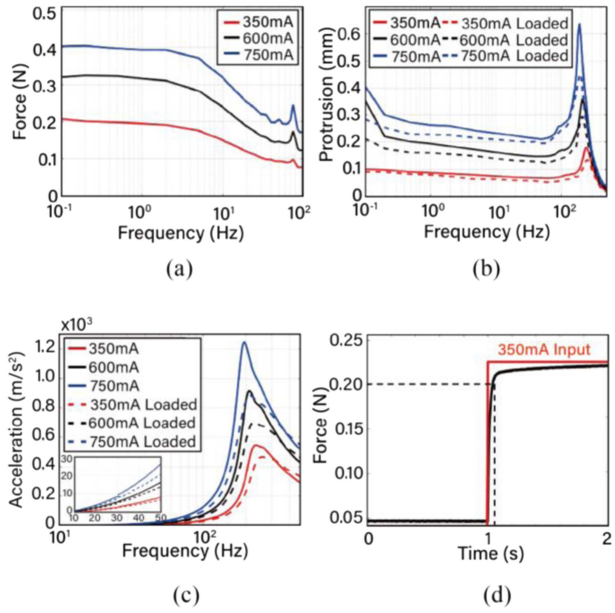

Fig. 6. Output performance of the actuator at input current amplitudes of 350, 600, and 750 mA for varying input signal frequencies: (a) Force response, (b) protrusion response showing resonance, and (c) acceleration response. (d) Step input response demonstrating the actuator's high dynamic performance with a low response time.

These experimental results demonstrate that the actuator is capable of generating rich and diverse tactile feedback, encompassing not only vibrations but also indentations, impulses, and complex haptic effects.

The actuator's response time was also examined. The time required to reach 90% of its maximum force output under a step input was 44.6 ms, as shown in Fig. 5(d), indicating a fast response suitable for real-time haptic rendering.

However, one limitation of the actuator is heat generation due to the high current passing through the coil. A thermal camera recorded a temperature rise to 40°C after 100 s of actuation at 100 Hz and 350 mA. However, since typical haptic interactions last no longer than 5 s, this heating is unlikely to pose a risk to the skin.

IV. User Test

A user study was conducted to assess the performance of the designed haptic display, specifically its ability to meet the perception threshold and enable users to identify and distinguish between multimodal tactile feedbacks. The study involved 12 participants—3 females and 9 males—ranging in age from 25 to 30 years (mean = 27.75, median = 27.5, SD = 1.76). All participants were right-handed and exhibited normal touch perception. This study was approved by the Institutional Review Board at the Korea Advanced Institute of Science and Technology (KH2023-177).

IEEE Robotics and Automation Letters (RA-L) paper, presented at ICRA 2026, Vienna, Austria. Cite as RA-L paper.

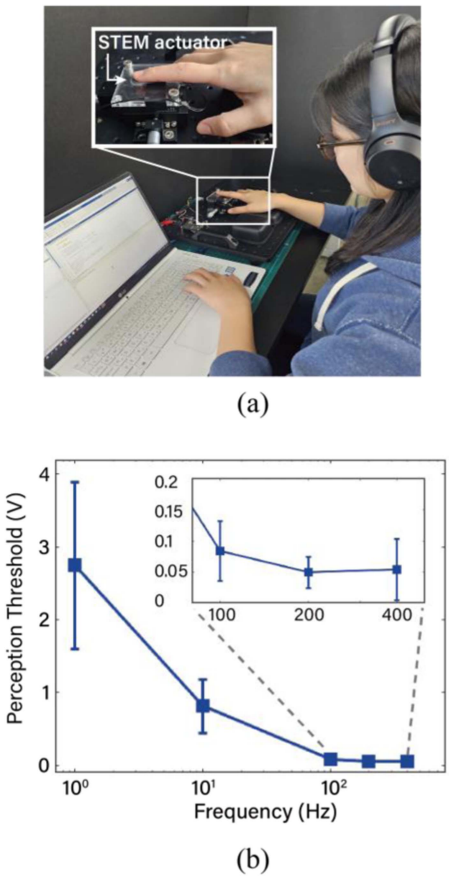

Fig. 7. (a) User test setup for measuring participants' perception thresholds. (b) Perception threshold levels, represented in terms of input voltage, for tactile feedback at 1, 10, 100, 200, and 400 Hz across 12 participants.

A. Absolute Threshold Test

The proposed actuator is capable of delivering not only protrusive force but also vibrations, including a combination of both, with varying frequencies. To determine the perception threshold for tactile feedback at different frequencies, the test procedure was designed as follows. As shown in Fig. 7(a), each subject rested their right hand on a supporting structure, with their index finger gently placed on the STEM actuator. Participants were instructed to rest their fingers lightly on the actuator without applying pressure. To eliminate auditory interference, all participants wore noise-canceling headphones playing pink noise throughout the experiment.

The experiment involved three trials at each actuation frequency: 1, 10, 100, 200, and 400 Hz. A "1-up 1-down adaptive staircase procedure" with a variable step size for input voltage was used, where the voltage was adjusted for ease of control. Each trial began with a stimulus well above the expected threshold. Participants were asked to respond with "yes" if they perceived the stimulus or "no" if they did not, using a laptop placed near their free hand. If the participant responded "yes," the intensity was reduced by a certain step size until the stimulus was no longer perceivable. When the user could no longer perceive the stimulus, the intensity was increased, and the step size halved from the previous decrement.

TABLE III
SENSITIVITY LEVELS AT DIFFERENT FREQUENCIES

Frequency (Hz)		10	100	200	400
SL (dB)	Input 350mA	3.32	41.81	53.30	53.13
	Input 600mA	9.15	48.35	61.16	55.96
	Input 750mA	12.69	52.28	64.55	57.37

This process continued until the participant responded with four reversals (alternating "yes" and "no") consecutively, indicating convergence at the threshold input voltage. To prevent infinite iterations, the maximum number of iterations was set to 25, with the entire test lasting around 20–30 min. Rest periods of 10 s between stimuli and 120 s between trials were allowed to prevent muscle fatigue.

The mean and standard deviation of the threshold values across all participants are shown in Fig. 7(b) for each frequency. As expected, participants exhibited lower threshold values at higher frequencies, with values of 0.049 V and 0.054 V for 200 Hz and 400 Hz, respectively. However, at lower frequencies, there was considerable variability among participants, reflecting individual differences in sensitivity to tactile stimuli, including static stimuli like indentation. Based on these threshold values, the sensitivity levels of the actuator's acceleration output under loaded state are summarized in Table III.

B. Identification Test of Tactile Feedbacks

To evaluate the multimodal capabilities of the actuator, which can generate a wide range of temporal and force variations, eight distinct tactile signals (S1–S8) were carefully designed. The input signals and the measured output force response are plotted in blue and black solid lines, and the signal's waveform are presented in Fig. 8(a). Each signal was selected to highlight specific tactile characteristics, including protrusive force (*S1* and *S2*), pulse-like force (*S3*), crisp step signals (*S4*), vibration (*S5* and *S6*), and combined waveforms with modulation effects (*S7* and *S8*).

The tactile signals and their waveforms can be categorized based on their distinct tactile sensations. *S1* and *S2* feature sinusoidal profiles with equal amplitude *A* but different cycle numbers, emphasizing protrusive force perception. *S3* and *S4* deliver sharp, pulse-like force feedback, where *S3* consists of two impulses $A\delta(t)$, and *S4* is a step-force signal $A[u(t) - u(t - T)]$, with both signals sharing same time period T. *S5* and *S6* provide low- and high-frequency vibrational feedbacks at frequencies $f_{low} = 25$ Hz and $f_{high} = 150$ Hz, respectively. Their intensities, A_{low} and A_{high}, are chosen such that both signals produce a similar acceleration output, ensuring comparable perceived vibration intensity. *S7* and *S8* incorporate modulation effects, where *S7* combines two sine functions to deliver protrusive force with vibration feedback, while *S8* features a vibrational waveform with an envelope, creating a beat-like sensation. Their average power input is described in Supplementary Material.

The signal pairs— *S1* & *S2, S3* & *S4, S6* & *S7*— can be differentiated based on their protrusive force characteristics. While *S5* and *S6* differ in frequency, *S7* and *S8* share similar amplitude modulation patterns but induce different perceived sensations due to their waveform structure. To prevent participants from

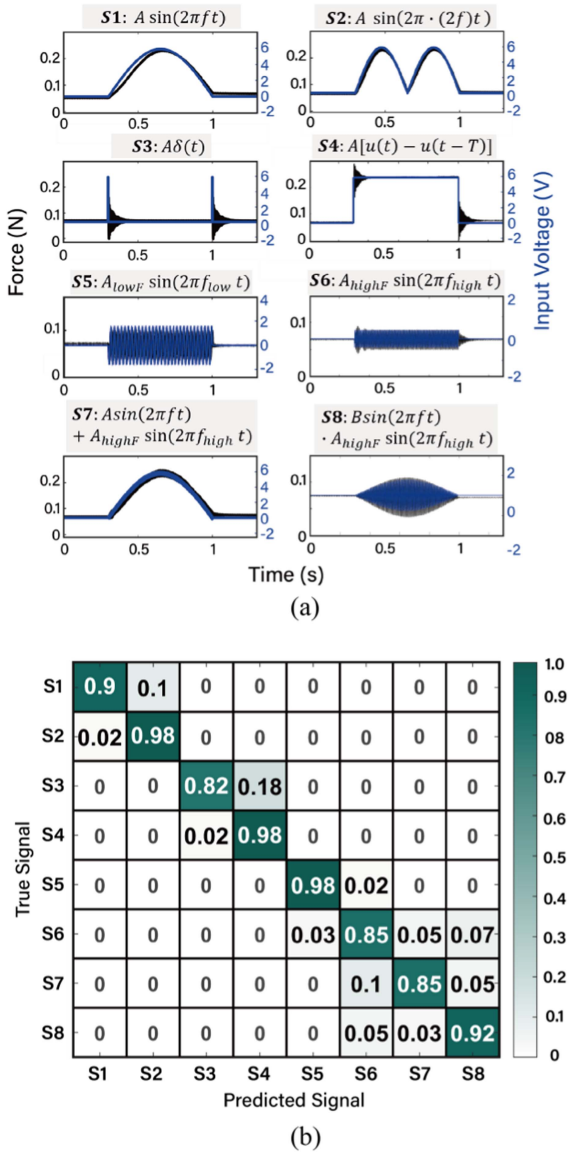

Fig. 8. (a) Eight distinct tactile signals used in the user identification test. (b) Confusion matrix representing the results of the user identification test.

identifying signals based on their duration, all signals were set to 0.7 seconds.

The user test setup mirrored that of the perception threshold measurement. Participants gently placed their index finger on the STEM actuator and responded using a PC with their free hand. Before the main experiment, participants underwent a learning phase during which they could freely explore and feel each of the eight signals until they were confident in identifying them. This phase lasted no more than 5 min.

The main experiment consisted of a randomized sequence of signals, with each signal being presented five times. Participants were tasked with identifying the 40 delivered signals and responding via the PC.

Their responses were recorded and analyzed, and the results were presented in a confusion matrix, as shown in Fig. 8(b). The matrix shows the normalized responses for each delivered signal. High values along the diagonal indicate that participants successfully identified the eight signals, with an average accuracy of 91%.

All 12 participants identified *S2, S4* and *S5* with high accuracy (98%), while minor confusion occurred between *S1* and *S2*, as well as between *S3* and *S4*. Due to the similar vibrational characteristics of *S6, S7* and *S8* with same frequency, participants exhibited errors in distinguishing these three tactile signals. The confusion primarily arose due to the weak protrusive force, making it challenging for some participants to differentiate the level of protrusion.

Despite these minor confusions, the results demonstrate that the actuator successfully delivered distinct tactile signals, achieving a high overall recognition rate.

V. Conclusion & Discussion

In this study, we developed a STEM actuator capable of delivering multimodal tactile feedback. By incorporating magnetic reinforcements, such as the soft magnetic cap and the ferromagnetic pole piece, we effectively amplified the output force by minimizing magnetic flux leakage. This enhancement was validated through both FEM simulations and experimental results. The actuator's performance was evaluated by measuring output force, protrusive displacement, and acceleration over a wide frequency range. Its ability to generate diverse feedback—including force, vibration, and impulse signals—demonstrates its versatility in comparison to traditional vibrotactile actuators. Furthermore, the integration of soft materials not only enhances wearability but also ensures sufficient force output for effective haptic rendering.

The user study showed that participants were able to reliably distinguish between eight different tactile signals, achieving an average accuracy of 91%. The highest recognition rates were observed for successive protrusive force, step, and low-frequency vibration feedback (*S2, S4* and *S5*), due to their distinct tactile characteristics. However, minor confusion was noted between high-frequency vibration with and without modulation (*S6, S7* and *S8*), which may be attributed to variations in the perception thresholds of protrusive force among participants. This finding suggests that optimizing signal amplitude and duration could further enhance the ability to differentiate similar stimuli.

Despite its strong performance, the actuator has some limitations. The heat generated by the electromagnetic coil during prolonged actuation may require additional thermal management to ensure user comfort during extended use. Additionally, while the actuator successfully delivers predefined signals, further research is needed to assess its adaptability to dynamic, real-time interactions and user-driven haptic feedback.

Future work will focus on leveraging the STEM actuator to enhance the immersiveness of VR environments by delivering realistic and dynamic haptic feedback. The actuator's ability to generate multimodal feedback can significantly improve the perception of virtual object and texture interactions. For instance, the actuator could simulate the sensation of pressing soft or rigid objects, or render the texture of rough or smooth surfaces with bumps with enhanced realism. These advancements will contribute to a richer, more intuitive VR experience, bridging the gap between visual perception and tactile interaction.

REFERENCES

[1] C. Wee, K. M. Yap, and W. N. Lim, "Haptic interfaces for virtual reality: Challenges and research directions," *IEEE Access*, vol. 9, pp. 112145–112162, 2021.

[2] C. Pacchierotti, S. Sinclair, M. Solazzi, A. Frisoli, V. Hayward, and D. Prattichizzo, "Wearable haptic systems for the fingertip and the hand: Taxonomy, review, and perspectives," *IEEE Trans. Haptics*, vol. 10, no. 4, pp. 580–600, Oct.–Dec. 2017.

[3] W. Dangxiao, G. Yuan, L. Shiyi, Y. Zhang, X. Weiliang, and X. Jing, "Haptic display for virtual reality: Progress and challenges," *Virtual Reality Intell. Hardware*, vol. 1, no. 2, pp. 136–162, 2019.

[4] B. Shneiderman, "Direct manipulation for comprehensible, predictable and controllable user interfaces," in *Proc. 2nd Int. Conf. Intell. User Interfaces*, 1997, pp. 33–39.

[5] V. Hayward, O. R. Astley, M. Cruz-Hernandez, D. Grant, and G. Robles-De-La-Torre, "Haptic interfaces and devices," *Sensor Rev.*, vol. 24, no. 1, pp. 16–29, 2004.

[6] T. N. Smyth and A. E. Kirkpatrick, "A new approach to haptic augmentation of the GUI," in *Proc. 8th Int. Conf. Multimodal Interfaces*, 2006, pp. 372–379.

[7] M. Speicher, J. Ehrlich, V. Gentile, D. Degraen, S. Sorce, and A. Krüger, "Pseudo-haptic controls for mid-air finger-based menu interaction," in *Proc. Extended Abstr. CHI Conf. Hum. Factors Comput. Syst.*, 2019, pp. 1–6.

[8] J. Yin, R. Hinchet, H. Shea, and C. Majidi, "Wearable soft technologies for haptic sensing and feedback," *Adv. Funct. Mater.*, vol. 31, no. 39, 2021, Art. no. 2007428.

[9] J. Martínez, A. García, M. Oliver, J. P. Molina, and P. González, "Identifying virtual 3D geometric shapes with a vibrotactile glove," *IEEE Comput. Graph. Appl.*, vol. 36, no. 1, pp. 42–51, Jan./Feb. 2016.

[10] P. Weber, E. Rueckert, R. Calandra, J. Peters, and P. Beckerle, "A low-cost sensor glove with vibrotactile feedback and multiple finger joint and hand motion sensing for human-robot interaction," in *Proc. 25th IEEE Int. Symp. Robot Hum. Interactive Commun.*, 2016, pp. 99–104.

[11] Y. Luo et al., "Adaptive tactile interaction transfer via digitally embroidered smart gloves," *Nature Commun.*, vol. 15, no. 1, 2024, Art. no. 868.

[12] "TactGlove," 2021. [Online]. Available: https://www.bhaptics.com/tactsuit/tactglove

[13] A. T. Maereg, A. Nagar, D. Reid, and E. L. Secco, "Wearable vibrotactile haptic device for stiffness discrimination during virtual interactions," *Front. Robot. AI*, vol. 4, 2017, Art. no. 42.

[14] V. Vechev, J. Zarate, D. Lindlbauer, R. Hinchet, H. Shea, and O. Hilliges, "Tactiles: Dual-mode low-power electromagnetic actuators for rendering continuous contact and spatial haptic patterns in VR," in *Proc. IEEE Conf. Virtual Reality 3D User Interfaces*, 2019, pp. 312–320.

[15] D. Leonardis, L. Tiseni, D. Chiaradia, and A. Frisoli, "A twisted string, flexure hinges approach for design of a wearable haptic thimble," *Actuators*, vol. 10, no. 9, 2021, Art. no. 211.

[16] H. Kim, M. Kim, and W. Lee, "HapThimble: A wearable haptic device towards usable virtual touch screen," in *Proc. 2016 CHI Conf. Hum. Factors Comput. Syst.*, 2016, pp. 3694–3705.

[17] S. B. Schorr and A. M. Okamura, "Fingertip tactile devices for virtual object manipulation and exploration," in *Proc. CHI Conf. Hum. Factors Comput. Syst.*, 2017, pp. 3115–3119.

[18] D. Wang, K. Ohnishi, and W. Xu, "Multimodal haptic display for virtual reality: A survey," *IEEE Trans. Ind. Electron.*, vol. 67, no. 1, pp. 610–623, Jan. 2020.

[19] M. Gabardi, M. Solazzi, D. Leonardis, and A. Frisoli, "A new wearable fingertip haptic interface for the rendering of virtual shapes and surface features," in *Proc. IEEE Haptics Symp.*, 2016, pp. 140–146.

[20] H. Kim, H. Yi, H. Lee, and W. Lee, "HapCube: A wearable tactile device to provide tangential and normal pseudo-force feedback on a fingertip," in *Proc. CHI Conf. Hum. Factors Comput. Syst.*, 2018, pp. 1–13.

[21] E. Leroy, R. Hinchet, and H. Shea, "Multimode hydraulically amplified electrostatic actuators for wearable haptics," *Adv. Mater.*, vol. 32, no. 36, 2020, Art. no. 2002564.

[22] H. Zhao et al., "A wearable soft haptic communicator based on dielectric elastomer actuators," *Soft Robot.*, vol. 7, no. 4, pp. 451–461, 2020.

[23] S. Mun et al., "Electro-active polymer based soft tactile interface for wearable devices," *IEEE Trans. haptics*, vol. 11, no. 1, pp. 15–21, Jan.–Mar. 2018.

[24] G. Frediani, H. Boys, M. Ghilardi, S. Poslad, J. J. Busfield, and F. Carpi, "A soft touch: Wearable tactile display of softness made of electroactive elastomers," *Adv. Mater. Technol.*, vol. 6, no. 6, 2021, Art. no. 2100016.

[25] J.-H. Youn, H. Mun, and K.-U. Kyung, "A wearable soft tactile actuator with high output force for fingertip interaction," *IEEE Access*, vol. 9, pp. 30206–30215, 2021.

[26] A. Talhan, H. Kim, and S. Jeon, "Tactile ring: Multi-mode finger-worn soft actuator for rich haptic feedback," *IEEE Access*, vol. 8, pp. 957–966, 2020.

[27] H. A. Sonar, J.-L. Huang, and J. Paik, "Soft touch using soft pneumatic actuator–skin as a wearable haptic feedback device," *Adv. Intell. Syst.*, vol. 3, no. 3, 2021, Art. no. 2000168.

[28] Z. Zhakypov and A. M. Okamura, "FingerPrint: A 3-D printed soft monolithic 4-degree-of-freedom fingertip haptic device with embedded actuation," in *Proc. IEEE 5th Int. Conf. Soft Robot.*, 2022, pp. 938–944.

[29] X. Yu et al., "Skin-integrated wireless haptic interfaces for virtual and augmented reality," *Nature*, vol. 575, no. 7783, pp. 473–479, 2019.

[30] D. Li et al., "Miniaturization of mechanical actuators in skin-integrated electronics for haptic interfaces," *Microsystems Nanoeng.*, vol. 7, no. 1, 2021, Art. no. 85.

[31] A. Panarese and B. B. Edin, "Human ability to discriminate direction of three-dimensional force stimuli applied to the finger pad," *J. Neurophysiol.*, vol. 105, no. 2, pp. 541–547, Feb. 2011, doi: 10.1152/jn.00322.2010.